



Technological University Dublin
ARROW@TU Dublin

Articles

School of Physics & Clinical & Optometric
Science

2017

The use of vibrational spectroscopy to study the pathogenesis of multiple sclerosis and other neurological conditions

Fiona Lyng

Technological University Dublin, Fiona.lyng@tudublin.ie

Inês R. Ramos

Sheffield Hallam University,

Ihtesham Ur Rehman

The Kroto Research Institute, Sheffield, UK;

Basil Sharrack

Sheffield Teaching Hospital Foundation Trust,

Nicola Woodroffe

Sheffield Hallam University,

Follow this and additional works at: <https://arrow.tudublin.ie/scschphyart>

Recommended Citation

Inês R. Ramos, et al. (2017) The use of vibrational spectroscopy to study the pathogenesis multiple sclerosis and other neurological conditions, *Applied Spectroscopy Reviews*, 52:10, 868-882, DOI: 10.1080/05704928.2017.1336450

This Article is brought to you for free and open access by the School of Physics & Clinical & Optometric Science at ARROW@TU Dublin. It has been accepted for inclusion in Articles by an authorized administrator of ARROW@TU Dublin. For more information, please contact yvonne.desmond@tudublin.ie, arrow.admin@tudublin.ie, brian.widdis@tudublin.ie.



This work is licensed under a [Creative Commons Attribution-Noncommercial-Share Alike 3.0 License](https://creativecommons.org/licenses/by-nc-sa/3.0/)



The use of vibrational spectroscopy to study the pathogenesis multiple sclerosis and other neurological conditions

Inês R. Ramos^a, Fiona M. Lyng^b, Ihtesham Ur Rehman^c, Basil Sharrack^{d,e} & M.

Nicola Woodroffe^a

^aBiomolecular Sciences Research Centre, Faculty of Health and Wellbeing, Sheffield Hallam University, Sheffield, UK; ^bDIT Centre for Radiation and Environmental Science, Focas Research Institute, Dublin Institute of Technology, Dublin, Ireland; ^cDepartment of Materials Science and Engineering, The Kroto Research Institute, Sheffield, UK; ^dSheffield Teaching Hospital Foundation Trust, Academic Department of Neurology; ^eThe University of Sheffield, Sheffield Institute for Translational Neuroscience and the Sheffield NIHR Biomedical Research Centre for Translational Neuroscience.

CORRESPONDING AUTHOR: Inês R. Ramos I.Ramos@shu.ac.uk Biomolecular Sciences Research Centre, Faculty of Health and Wellbeing, Sheffield Hallam University, Owen Building, City Campus, Howard Street, Sheffield, S1 1WB, UK.

RUNNING HEAD: Spectroscopy for multiple sclerosis

KEYWORDS: Multiple sclerosis, normal-appearing white matter, pathology, spectroscopy

1 **Abstract**

2 Spectroscopy techniques are valuable tools in biomedical research and have been used
3 extensively in the study of disease. However, neurological conditions such as multiple
4 sclerosis (MS) have received little attention and the available spectroscopy studies are
5 limited, both in overall numbers of patients studied and the disease samples considered. MS
6 is a complex immune-mediated disease, with variable clinical courses and limited
7 therapeutic options. This review aims to summarize current literature in the area,
8 demonstrating how spectroscopy techniques can provide valuable information to inform and
9 advance research into the most common neurological condition affecting young adults.

10 Introduction

11 Biophotonic techniques are now widely used in biomedical research targeting better
12 diagnosis, prognosis and surveillance of disease. Vibrational spectroscopy methods such as
13 Fourier-transform infrared (FTIR) and Raman spectroscopy are so called because they
14 probe the intramolecular vibrations and rotations of a sample when irradiated with a light
15 source (1). The vibrational energy levels can be probed by both techniques, using different
16 physical processes. Raman spectroscopy studies the Raman effect, the spontaneous
17 inelastic light scattering process of photons, following the interaction of monochromatic
18 radiation (e.g. a laser) with the sample. In contrast, FTIR spectroscopy studies the samples'
19 absorption characteristics arising from the molecular motion due to atomic displacement
20 upon interaction with an infrared source (2, 3). In both cases, the recording of vibrational
21 energy level transactions results in a spectrum composed of peaks/bands that can be
22 interpreted qualitatively (peak position) and quantitatively (peak intensity/area) (4). In FTIR
23 spectroscopy, the spectral bands arise from a change in the electric dipole moment of the
24 molecules, whereas in Raman spectroscopy, they arise from a change in molecular
25 polarizability. FTIR and Raman spectroscopies are therefore complementary and provide a
26 "fingerprint" or "signature" of the specific molecules contained within a biological sample
27 (proteins, lipids, DNA), depending upon whether their bonds exhibit infrared or Raman
28 activities. Both FTIR and Raman can be used for imaging tissue sections and are non-
29 destructive, label-free techniques with sub-micron spatial resolution (5).

30 In biomedical research, scientists are continually investigating and exploring the application
31 of new technologies that can detect early signs of disease and thereby reduce disease
32 morbidity and mortality. The detection of biomarkers plays an important role in this
33 exploration. In oncology, such biomarkers, have been used extensively to determine risk
34 factors, aid diagnosis and prognosis, and in the assessment of treatment response as well
35 as determining disease recurrence (4). However, from amongst the vast numbers of
36 candidate biomarkers, only a limited few have been validated for clinical use. Vibrational
37 spectroscopy is new investigatory tool in biomarker (re)search which is not restricted to the
38 analysis of a specific protein, nucleic acid and/or lipid. As such, FTIR and Raman spectra
39 are able to give spectral "signatures" or "biomarkers" which reflect the overall molecular
40 composition of the studied samples (4).

41 Despite being extensively used in the field of cancer research (6, 7), FTIR and Raman
42 spectroscopy are currently under explored in the study of diseases which affect the central
43 nervous system (CNS) including multiple sclerosis (MS). To date, there are very few
44 published papers in this field including a review article published in 2012 (8).

45 **Multiple Sclerosis (MS)**

46 MS is considered to be an autoimmune, neuro-inflammatory and degenerative condition,
47 which affects both the brain and spinal cord. Its precise aetiology remains unknown,
48 although both genetic and environmental factors influence an individual's susceptibility to
49 develop MS (9). The clinical course of this disease is variable but is divided into several
50 categories reflecting the degree of clinical disease activity and disability progression rate,
51 including relapsing remitting (RRMS), primary progressive (PPMS) and secondary
52 progressive MS (SPMS) (10). Whilst the inflammatory component of MS pathogenesis is
53 relatively well understood, the progressive neurodegenerative component of the disease, in
54 both its primary and secondary progressive clinical courses, is yet to be elucidated. In
55 PPMS, patients have a gradual and progressive decline in function from the outset, with
56 minimal disease activity detectable on magnetic resonance imaging (MRI) whereas in
57 SPMS, the gradual progression follows an initial relapsing remitting phase, usually over
58 many years (11). The consensus is that MS is a spectrum of conditions with RRMS being
59 one end of that spectrum and PPMS being at the other.

60 The key pathological features observed in MS are the influx of inflammatory immune cells
61 across the blood brain barrier into the CNS which results in the loss of axons and their
62 insulating myelin sheaths and the formation of lesions (plaques) in the white matter (WM)
63 and to a lesser extent in the grey matter (12). This process results in the impairment of
64 conduction along the affected axon leading to variable symptoms experienced by affected
65 patients including cognitive impairment, visual disturbances, sensory and motor symptoms,
66 impaired balance, sphincter disturbance and fatigue (13). Histopathological comparisons of
67 CNS tissue shows that the classical perivascular inflammation seen in SPMS is much less
68 prominent in PPMS and that more diffuse inflammatory changes and greater extent of
69 axonal damage in the normal appearing white matter (NAWM) are seen in PPMS (14, 15). In
70 addition, there is evidence that patients with PPMS have a reduced capacity for re-
71 myelination (11). Understanding the underlying pathogenesis which underpins the clinical
72 progression in MS at the molecular and cellular levels is therefore vital for the development
73 of therapies targeting the neurodegenerative process and enhancing remyelination
74 strategies.

75 The diagnosis of MS is usually based on the clinical presentation and the results of brain and
76 spinal MRI, which reveals evidence of active and chronic lesions as well as focal and
77 generalised atrophy (16). Current treatments for MS target the initial relapsing phase of the
78 disease, by preventing inflammatory responses leading to a reduction in the number and
79 severity of relapses (17). However, there are currently no treatments for primary and

80 secondary progressive MS although two therapeutic agents are waiting to be licenced (18). .
81 The underlying pathogenesis of the initial inflammatory phase of MS has been well
82 characterised at both the cellular and molecular level. However the pathogenesis of the
83 progressive phase is still not fully elucidated, although changes in the NAWM appear to be
84 pivotal (12). The progressive loss of axons seem to continues despite the reduction of
85 relapses with the use of effective anti-inflammatory therapies resulting in irreversible
86 disability which support the presence of two separate pathological processes: inflammation
87 and neurodegeneration (19).

88 Approaches to studying MS pathogenesis have focussed on the analysis of post-mortem
89 CNS tissue, as well as experimental work using both primary CNS cells such as astrocytes,
90 microglia and oligodendrocytes isolated from CNS tissue, which allows manipulation of the
91 individual cell's environment. In addition, a number of animal models of MS have been
92 developed, primarily in rodents but also in primates, in order to investigate the disease
93 course of MS. In these animals, experimental autoimmune encephalomyelitis (EAE) is
94 induced through the injection of spinal cord homogenates, myelin proteins or peptides, such
95 as myelin oligodendrocyte glycoprotein (MOG), myelin basic protein (MBP) or proteolipid
96 protein (PLP), in addition to adjuvant. This promotes the induction of an autoimmune
97 response against myelin, leading to both an inflammatory response in the CNS as well as,
98 dependent on the model used, demyelination (20). Nevertheless, the progressive aspects of
99 the human condition seen in MS are more difficult to reproduce in animal models (21),
100 although Peferoen has recently described an EAE model in Biozzi mice which, dependent on
101 the age of the mouse at induction of disease, demonstrates progressive disease, with
102 younger mice having an initial relapsing remitting phase followed by a secondary
103 progressive phase and older mice showing progression at onset of disease induction (22). A
104 further drawback of these animal models is that off the multitude of therapies found to be
105 effective in preventing EAE, a very small number have been taken forward into clinical trials
106 (23), suggesting that the models do not fully mimic the pathogenesis of MS in humans.

107 Current research approaches to investigating the aetiology of MS focus on the search for
108 specific genes/proteins/lipids that are thought to be involved in the disease process using a
109 variety of cell and molecular biology approaches. More recently DNA microarrays have been
110 used to assess more global changes in gene expression in MS diseased human CNS tissue
111 compared with normal age matched control (24, 25). The application of proteomic and
112 metabolomic analyses in MS have focussed on biomarkers in biological fluids, including
113 blood, cerebrospinal fluid and urine rather than in MS CNS tissue (26, 27).

114 The advantage of Raman and FTIR for analysis of human tissues is that the overall chemical
115 composition of the tissue in terms of lipids, nucleic acids and proteins is obtained.
116 Spectroscopic study of MS has been reported in the literature using both human post-
117 mortem CNS tissue and animal models of the disease. A review of all available original
118 research articles published to date is provided below and is summarized in Table 1.

119

120 **Human CNS tissue spectroscopy studies**

121 Initial studies applying spectroscopic techniques to the study of MS pathology were reported
122 in the 1990s. Choo *et al.* were the first to use FTIR to study human white and grey matter
123 tissue, obtained from healthy control subjects, and compared it with MS demyelinated
124 lesions tissue from MS patients (28). This rapid communication reported that it was possible
125 to discriminate between different types of MS tissue attributed to variations in intrinsic lipid
126 and water content. Whilst FTIR spectra of white matter was dominated by lipids and protein
127 absorptions and grey matter spectra showed reduced lipid content alongside an increase
128 contribution of water to the spectra; MS lesion spectra were suggestive of both lipid and
129 water depletion, as would be expected from histopathological tissue analysis (28).

130 Differences comparing white and grey matter as well as white matter with MS lesions were
131 most notable in the 2800-3000 cm^{-1} spectral region, where most infrared bands arise from
132 CH_2 and CH_3 stretching vibrations of lipid acyl chains. Four main assignments were made to
133 CH_3 and CH_2 asymmetric stretching vibrations at 2956 and 2922 cm^{-1} and, to symmetric
134 vibrations at 2871 and 2851 cm^{-1} respectively. The overall intensity of these peaks were
135 reduced in both grey matter and MS lesion tissue, compared to normal control white matter,
136 which the authors explained was due to the expected lower lipid content of grey matter and
137 MS lesions, due to demyelination. Similarly, the CH_2/CH_3 ratio is also decreased as a
138 decrease in lipid to protein ratio leads to methylene and methyl groups of amino-acid side
139 chains dominating this spectral region; as the CH_2/CH_3 ratio in proteins is much lower than in
140 lipids, it was expected that the overall ratio would be decreased and band broadening would
141 be observed. In order to distinguish between grey matter and MS lesion tissue, the authors
142 reported the spectral region of 1200-1800 cm^{-1} to be most useful (28).

143 The main feature in white matter' spectra was observed at 1467 cm^{-1} and assigned to the
144 scissoring vibration of CH_2 groups of lipid acyl chains. In grey matter, the intensity absorption
145 of this CH_2 scissoring is reduced and is almost equal to the CH_3 asymmetric bending
146 vibrations at 1456 cm^{-1} . This is explained by the reduction in lipid content, which is also

147 apparent by the decrease in intensity of the terminal methyl groups of lipid chains and of the
148 $(\text{CH}_3)_3\text{N}^+$ symmetric bending of phosphatidylcholine headgroups, assigned to the bands at
149 1381 and 1415 cm^{-1} , respectively. In contrast the COO^- symmetric stretching band at 1400
150 cm^{-1} is increased in the spectra of grey matter in comparison to white matter. The same was
151 also observed at 1308 cm^{-1} which the authors assigned to amide III(28).

152 The spectral features of MS plaque tissue are similar to the ones described for grey matter.
153 Nevertheless, the intensity of CH_2 scissoring (1467 cm^{-1}) to CH_3 asymmetric bending
154 vibrations (1456 cm^{-1}) is now reversed with CH_3 asymmetric bending vibrations being the
155 main feature in this region. Similarly, the PO_2^- antisymmetric stretching band also displays
156 greater intensity in the plaques' spectra comparatively to grey matter. Both these
157 observations were suggested to indicate that lipid content of MS plaques is lower than that of
158 the grey matter (28), which is known to be the case from histopathology studies (13).

159 In the 1500 to 11800 cm^{-1} spectral range the main feature observed was the amide I band
160 which arises from the $\text{C}=\text{O}$ stretching vibration of amide groups of proteins and is centred at
161 1653 cm^{-1} . Other absorptions reported were assigned to $\text{C}-\text{C}$ stretching of tyrosine at 1517
162 cm^{-1} ; the amide II band centred at 1550 cm^{-1} ; and the acidic amino-acid and arginine side
163 chains at 1581 and $1580-1610\text{ cm}^{-1}$ respectively. In addition, the ratio of amide I to amide II
164 was increased comparatively to that of isolated proteins. It was suggested this may result
165 from non-protein contributions to the amide I region, and further proposing water to be the
166 main source of this contribution (28).

167 Le Vine *et al.* (1998) assessed active lesions in MS tissue compared with healthy control
168 white matter and reported an increased oxidation state of both lipids and proteins in MS
169 lesions, indicative of a role for free radicals in MS pathogenesis (29). The spectra of WM
170 tissue from control post-mortem cases was dominated by CH_2 absorptions at 2923 and 1468
171 cm^{-1} , $\text{P}=\text{O}$ at 1235 cm^{-1} and $\text{HO}-\text{C}-\text{H}$ at 1060 cm^{-1} , characteristic of lipids, phospholipids and
172 glycolipids respectively. Areas of NAWM within MS cases were reported to display similar
173 spectra to normal control white matter, whereas lesion areas display significant changes,
174 such as a reduced ratio of CH_2 to NH and OH , in comparison with control white matter.
175 Further differences were revealed by the investigation of the oxidation products of lipids and
176 proteins. Previous studies reported the amide I peak at $\sim 1660\text{ cm}^{-1}$ to be broader when
177 proteins are oxidised and the carbonyl absorption at 1740 cm^{-1} to be increased when lipids
178 are oxidised. This study reported the $\text{C}=\text{O}$ (1740 cm^{-1}) to CH_2 (1468 cm^{-1}) ratio to be
179 increased and the peak at 1657 cm^{-1} to be broader in MS lesions in comparison with white
180 matter from control samples (29).

181 Furthermore, the authors followed the spatial spectroscopic profiles of these features by
182 recording linear maps acquired partially or wholly within MS lesions sites and representative
183 areas of control white matter. They reported the CH₂ (1468 cm⁻¹) to amide II (1544 cm⁻¹) ratio
184 to be 0.644±0.053 for control samples (n=5), ranging from less than 0.1 to 0.7 in MS ones
185 (n=5); 15.950±1.593 was the mean of the C=O (1740 cm⁻¹) to amide II (1544 cm⁻¹) ratio in
186 control cases, which was in turn decreased for all MS cases; and four out of five MS cases
187 presented one or more values above the mean of 24.047±3.22 for C=O (1740 cm⁻¹) to CH₂
188 (1468 cm⁻¹) ratio of control samples. Finally, whilst controls displayed an average of -
189 0.033±0.010 at 1652 cm⁻¹, MS cases displayed greater values all above -0.02 (29).

190 It was concluded that the higher carbonyl to CH₂ ratio detected in the spectra of MS cases is
191 suggestive of lipids being oxidised, whilst oxidation of proteins cause the 1657 cm⁻¹ peak to
192 broaden to 1652 cm⁻¹ in MS plaque tissue. This result may be caused by gliosis, which
193 occurs in parallel with the demyelination process leading to higher expression of glial
194 fibrillary acidic protein by astrocytes, which was also indicated as a potential factor
195 contributing to the amide I broadening, as well as the relative greater expression of amide II
196 (29).

197 More recently, Poon *et al.* used Coherent Anti-Stokes Raman Scattering (CARS) to study
198 several regions of post-mortem MS brain, including areas of NAWM, remyelination and both
199 active and chronic lesions (30). Investigating five chronic MS cases, they reported a novel
200 instrument that allows acquisition of high resolution, label-free imaging whose pixels contain
201 spectral information, together with a post-processing method, which allows isolation and
202 quantification of these spectral images. The study showed the CH₂ symmetric stretch of
203 2850 cm⁻¹ in NAWM, to shift to 2885 cm⁻¹ when myelin was contained within the phagocytic
204 macrophages/microglia cells within the tissue (a CARS image is overlaid with
205 immunostaining with the marker HLA-DR/LN3, confirming activated microglia). This was
206 proposed to arise from the intermolecular chain disorder resulting from the breakdown of the
207 myelin components during demyelination. Further CARS pseudo-colour images showed
208 myelinated axons to have greatly reduced density within remyelinated areas in active lesion
209 sites (30).

210 An additional study, also by Poon *et al.* reported lipid biochemical changes preceding myelin
211 protein loss in peri-lesional areas and NAWM, when inspecting the CH spectral region from
212 2750 to 3100 cm⁻¹ (31). CARS images were acquired from the NAWM region adjacent to the
213 lesion and sequential images were acquired moving away from the lesion into the NAWM..
214 Triplicate images were also acquired from an area furthest away from the lesion site,
215 referred to as "true NAWM" and from matched brain regions in tissue sections from control

216 non-MS cases. The average "true NAWM" spectra did not overlap with region-matched
217 control spectra, suggesting possible underlying pathology in MS tissue, which is not
218 differentiated when using lipophilic histochemistry or immunostaining with conventional
219 techniques (31).

220 The three major features in the CH spectral region analysed, correspond to the symmetric
221 and asymmetric and asymmetric stretching of acyl chain methylene at 2850 and 2886 cm^{-1}
222 respectively, and the CH_3 methyl chain end symmetric stretch at 2935 cm^{-1} , which is thought
223 to include protein contributions as well. Observing the intensity ratios of 2850/2880 cm^{-1} and
224 2935/2880 cm^{-1} the authors noted a slowing decreasing trend across all measured intensity
225 ratios, when moving away from the lesion site until reaching the "true NAWM" ratios,
226 recorded from an area the furthest away from the lesion, and approaching the ratios of
227 region-matched non-MS control samples. The 2850/2880 cm^{-1} ratio is thought to relate to the
228 intermolecular packing, interchain interactions and intrachain torsional motions, whereas the
229 2935/2880 cm^{-1} ratio allows monitoring intramolecular chain disorder and trans-gauche
230 isomerisation. The authors conclude that biochemistry of myelin lipid content changes in the
231 lesion periphery and in NAWM (31).

232 **Mouse models of demyelination and remyelination**

233 Animal models of MS have also been investigated by vibrational spectroscopy, where most
234 studies aim to elucidate the mechanisms behind demyelination and remyelination. Heraud *et*
235 *al.* used FTIR spectroscopy to investigate macromolecular components and protein
236 conformational changes in the CNS of EAE versus control tissue sections(32). Using
237 principal component analysis (PCA) and artificial neuronal networks (ANN) to analyse single
238 data acquisition spectra, the authors demonstrated, without the need for chemical stains,
239 subtle chemical and structural changes, particularly in the secondary structure of proteins in
240 the white matter (33).

241 Fu *et al.* used resonant CARS imaging from the symmetric CH_2 stretch vibration at 2840 cm^{-1}
242 to characterize myelin changes induced by lysophosphatidyl choline (lyso-PtdCho) (34).
243 Although not directly relevant to demyelinating diseases including MS, the authors reported
244 CARS was able to characterise the changes occurring in lyso-PtdCho-induced myelin
245 breakdown and that together with electrophysiological data, it revealed involvement of a
246 Ca^{2+} , calpain, and cPLA₂-dependent pathway (34).

247 In another study, CARS was used to study myelin loss in the mouse-model, Relapsing-EAE
248 (R-EAE) (35). Two theories have been hypothesised for initiating demyelination, one where

249 the injury starts at internodal myelin, thinning layer by layer and the other, where it initiates
250 with paranodal domain injury. The authors noted that the submicron spatial resolution of
251 CARS images allowed not only the quantification of myelin thickness but also the ratio of
252 myelin thickness to the axonal diameter at different stages of the disease process.
253 Furthermore, two-photon immunofluorescence microscopy revealed that juxtaparanodal K⁺
254 channels, paranodal myelin retraction and the displacement of K⁺ channels was extensively
255 observed at the onset of R-EAE and at lesion borders. Overall their results suggested loss of
256 nodal integrity precedes the formation of myelin debris in the CD4⁺ T-cell-mediated R-EAE
257 model of MS and that remyelination is accompanied by reestablishment of the nodal makers,
258 with myelin being only partially restored (35).

259 Furthermore, the Raman spectra of myelin were dominated by lipid assignments and the
260 authors studied both C-C and C-H vibrational bands to determine the conformation of their
261 hydrocarbon chains through: (1) lipid packing studied using prominent bands at 2850, 2885
262 and 2930 cm⁻¹, assigned respectively to stretching and asymmetric stretching of CH₂ and to
263 CH₃ stretching: and, (2) lipid unsaturation using the ¹1650/¹1445 ratio, which represents the
264 C=C stretching bands to H-C-H deformation bands in lipid acyl chains. Myelin debris
265 presented a higher intensity of the ¹2930/¹2885 ratio, reflecting an increased intermolecular
266 chain disorder; and regenerated myelin presented a higher lipid-packing disorder than
267 normal myelin. Similarly, myelin debris presented the highest unsaturation degree, which
268 was decreased in regenerated myelin but nevertheless was higher than normal myelin.
269 Finally, the analysis of the ¹1122/¹1076 ratio, revealed no significant change could be
270 observed in the intramolecular chain ordering of myelin debris, normal and regenerated
271 myelin (35).

272 A non-invasive multimodal CARS system, combining reflectance for visualizing axons,
273 fluorescence to visualize green fluorescence protein (GFP) and Raman to visualize myelin
274 and to monitor microglia induced neurodegeneration was reported by Imitola *et al.* (36).
275 Using an EAE model, the authors reported fast *ex vivo* imaging of myelin, axons and
276 microglia with great anatomical precision in live tissue. CARS images showed a global
277 decrease in myelination, not seen before through other imaging techniques. This suggests
278 that subtle alterations in the myelin lipid content may precede hallmark CNS demyelination,
279 which is correlated with axonal loss and microglia activation (36).

280 Wang *et al.* reported DBT (3,3'-diethylthiatricarbocyanine iodide) to be a promising probe for
281 Near Infrared Fluorescence (NIRF) imaging of myelination (37). Through *in vivo* NIRF
282 studies on hyper and hypomyelination mouse models, the authors demonstrated DBT
283 successfully enters the brain and selectively binds to myelin sheaths. Furthermore, aiming to

284 broaden NIRF-DBT imaging to MS disease, the authors studied a cuprizone-induced mouse
285 model for demyelination and remyelination. NIRF imaging and quantitative analysis revealed
286 DBT could successfully monitor the level of demyelination and subsequent remyelination in
287 this mouse model, that could be correlated with histochemical staining (37).

288 **Future research directions**

289 The current literature, as reviewed above, considering human post-mortem CNS tissue
290 specimens is limited, with most studies considering a nominal sample number as shown in
291 Table 1, which also summarises the studies completed in models of MS.

292 Studies focusing on animal models have shown spectroscopy to be a valuable tool in
293 probing the biochemical composition of samples otherwise deemed identical. The spectral
294 imaging of myelinating and remyelinating processes, for example, further demonstrated the
295 ability to differentiate between newly formed myelin and endogenous myelin, indicating the
296 remyelinating process generates myelin of a different composition. Nonetheless, studies
297 considering human samples are limited and concern only a small number of post-mortem
298 tissues as human CNS material is difficult to obtain. Furthermore, most studies focused on
299 the spectral distinction of MS lesions from control tissue of non-diseased subjects, which can
300 readily be achieved by macro and microscopic evaluation using luxol-fast blue (LFB) stain or
301 immunohistochemistry for myelin proteins to examine demyelination. As disease diagnosis
302 through tissue sampling is not feasible, the advantages of spectroscopy techniques such as
303 FTIR and Raman rely on their ability to reveal underlying biochemical changes not yet
304 detectable either macro or microscopically, for example on NAWM of MS cases, when
305 common techniques fail to recognize differences. Spectral data could potentially help to
306 understand the underpinning mechanisms of disease and advance research in the field by
307 probing deeper into the chemical composition of apparently normal areas of MS cases.

308 **FTIR and Raman spectroscopy analysis of post-mortem white matter MS tissue: 309 NAWM has a different signature**

310 Analysing four post-mortem brain samples obtained from UK MS Society Tissue Bank
311 (Imperial College London) we show FTIR signatures allow the distinction of normal control
312 WM from both active and chronic lesions, and more interestingly from the NAWM of MS
313 cases despite no visible demyelination being observed when staining NAWM with LFB. The
314 mean FTIR spectra of a brain tissue sample from control, NAWM, active lesion and a chronic
315 lesion are represented in Figure 1, where it is possible to observe that the symmetric and
316 anti-symmetric C-H stretches attributed to lipids $\sim 2800-3000\text{ cm}^{-1}$ gradually decrease from

317 control to active lesion, as do the C-O and P-O stretches attributed to nucleic acids after
318 1000 cm^{-1} .

319 This decrease in lipid content seems to be in line with the previous findings acknowledged in
320 this review of published work and is in agreement with the well characterised process of
321 demyelination which occurs in MS, providing support to the validity of this approach to the
322 study of the biochemical composition of brain tissue in MS.

323 Principal Component Analysis (PCA) was further employed to highlight the variability existing
324 in the recorded spectral data set. PCA of FTIR signatures allowed the distinction of normal
325 control WM from both active and chronic lesions, as expected, but also differentiated NAWM
326 of the MS cases from control white matter cases. 2-D PCA scatterplot is shown in Figure 2.

327 A clear distinction between all sample groups can be observed. If the distinction between
328 control and chronic and active lesions were expected due to MS pathology, the separation
329 between NAWM and control WM provides novel insights into the alterations in white matter
330 in MS which might contribute to disease progression.

331 PCA was also employed to compare FTIR data from NAWM and control white matter
332 samples and results are shown in Figure 3. Figure 3A indicates that NAWM and control
333 white matter FTIR spectra separate according to the 1st principal component (PC1) which
334 accounts for 80.63% of the variation observed within the data set. The PC1 loading
335 represented in Figure 3B shows that this separation is dominated by the negative loading of
336 two main lipid assignments $\sim 2800\text{-}3000\text{cm}^{-1}$ indicating these are more intense in the control
337 WM samples (in black on the negative part of the PCA plot (Figure 3A)).

338 These preliminary results demonstrate that FTIR spectroscopy can be applied to analysis of
339 post-mortem WM tissue and successfully discriminate not only between lesion and control
340 WM but also between NAWM and control, without requiring any additional techniques.
341 Furthermore, they are suggestive of a significant decrease in lipid content in NAWM tissue in
342 MS cases, which is not detected by current staining techniques or documented in the
343 literature, but ought to be further investigated to better understand MS pathogenesis and the
344 biochemical changes that lead to lesion formation. Finally, the spectral signatures of the
345 fingerprint region also pointed to additional differences at the protein and nucleic acid level;
346 these pose further questions as to which specific species (i.e. proteins) are being 'lost' in
347 NAWM samples, which could contribute to the disease process.

348 Similarly, the samples were also analysed using a Horiba XploRA PLUS confocal Raman
349 microscope, operating with 532nm laser light and 1800nm lines grating. Raman signatures

350 of the fingerprint region were analysed using PCA and results are shown in Figure 4. PCA
351 score plots, in Figure 4A, showed the separation of NAWM (black) and control WM (green)
352 only to be achieved on the third PC which account for approximately 2% of the variance
353 found within the dataset. PC 1 and 3 loadings are shown in Figure 4B. Our group is
354 currently investigating the Raman signatures of NAWM samples further and a full research
355 paper will be published in due course.

356 **FTIR and Raman spectroscopy analysis of biofluids**

357 Much like tissues, biofluids exhibit vibrational spectra that have characteristic bands
358 reflecting their bimolecular composition (4). There are several reports of the application of
359 Raman and FTIR spectroscopy to the study of body fluids. Although blood and serum are
360 most commonly used due to their easy, less-invasive availability other biofluids including
361 cerebrospinal fluid (CSF), bile, urine, saliva, pancreatic juice, synovial and pleural fluids,
362 which are considered to more closely reflect ongoing pathology in the associated diseased
363 tissue, have also been studied. In Alzheimer's disease, serum data from Raman
364 spectroscopy allowed differentiation of Alzheimer's patients from other dementia cases (38),
365 whereas in a different study, plasma spectral data was used to grade mild, moderate and
366 severe Alzheimer's disease cases (39). FTIR spectroscopy showed Alzheimer's patients'
367 plasma samples to be well delineated from normal ageing subjects (40) and the same was
368 demonstrated for CSF (41). More recently, PCA-LDA allowed the distinction of the different
369 types of mild, moderate and severe Alzheimer's disease cases and controls, with 85%
370 accuracy, when using white blood cells from patients, using FTIR spectra and about 77%
371 when using the plasma spectra. These 83% accuracy values increased to 83 and 89% when
372 only moderate and severe patient groups were being considered (42).

373 FTIR spectroscopy analysis of synovial fluid has been shown to allow differentiation of joints
374 affected by rheumatoid arthritis, osteoarthritis, spondyloarthropathies and meniscal
375 injuries(43); whereas a Raman study showed the ability to discriminate patients with low and
376 high osteoarthritis severity (44). More recently, FTIR analysis of blood plasma for diagnosis
377 of schizophrenia and bipolar disorders against a healthy control group has also been
378 reported (45). A separation of all sample groups was observed using PCA, with assignments
379 to lipids from lipoproteins, polypeptides, and phosphates associated to the DNA backbone
380 being responsible for the separation; whilst PLS-DA allowed for the correct classification of
381 all sample groups. Sensitivity and specificity results were highest when the full spectral
382 range was considered, being respectively 100 and 100% for schizophrenia and 100 and
383 84.6% for bipolar disorder.

384 Overall, as demonstrated in this review and from our own FTIR preliminary data,
385 spectroscopic techniques have the potential to advance our knowledge of MS pathogenesis.
386 The analysis of post-mortem material, especially the comparison between NAWM and
387 normal WM can provide insights into molecular changes unveiling novel disease
388 mechanisms. And, although currently it cannot be applied for diagnostic purposes, due to the
389 constraints of obtaining brain tissue specimens, other patient specimen samples such as
390 CSF and blood might prove useful in the future to achieve a more rapid and accurate
391 diagnosis and prognosis for people with MS, much like has been recently reported for other
392 CNS diseases such as Alzheimer's.

393 **Conclusion**

394 The understanding of the underlying mechanism that lead to disease pathology and specially
395 disease progression is of great importance in neurodegenerative conditions, such as MS.
396 Spectroscopy techniques have the ability to unbiased characterisation of the biochemical
397 composition of post-mortem and clinical samples alike, thus able of providing insights into
398 the underlying changes occurring in tissue and biofluids (i.e. blood and CSF) which in turn
399 could be helpful to guide future *in vitro* research aimed at novel therapeutics.

400 **Acknowledgements**

401 The authors would like to acknowledge the UK MS Society Tissue Bank for providing the
402 tissue samples for preliminary FTIR and Raman spectroscopy analysis and Dr Rachel Waller
403 for sectioning and staining the samples.

404 **References**

- 405 1. Lasch, P., and Kneipp, J. (2007) *Biomedical Vibrational Spectroscopy*.
- 406 2. Dumas, P., Sockalingum, G. D., and Sulé-Suso, J. (2007) Adding synchrotron
407 radiation to infrared microspectroscopy: what's new in biomedical applications?
408 *Trends Biotechnol.* 25 (1): 40–44.
- 409 3. Baker, M. J., Trevisan, J., Bassan, P., Bhargava, R., Butler, H. J., Dorling, K. M.,
410 Fielden, P. R., Fogarty, S. W., Fullwood, N. J., Heys, K. a, Hughes, C., Lasch, P.,
411 Martin-Hirsch, P. L., Obinaju, B., Sockalingum, G. D., Sulé-Suso, J., Strong, R. J.,
412 Walsh, M. J., Wood, B. R., Gardner, P., and Martin, F. L. (2014) Using Fourier
413 transform IR spectroscopy to analyze biological materials. *Nat. Protoc.* 9 (8): 1771–
414 91.
- 415 4. Baker, M. J., Hussain, S. R., Lovergne, L., Untereiner, V., Hughes, C., Lukaszewski,
416 R. A., Thiéfin, G., and Sockalingum, G. D. (2016) Developing and understanding
417 biofluid vibrational spectroscopy: a critical review. *Chem. Soc. Rev.*
- 418 5. Krafft, C., Dietzek, B., Schmitt, M., and Popp, J. (2012) Raman and coherent anti-
419 Stokes Raman scattering microspectroscopy for biomedical applications. *J. Biomed.*
420 *Opt.* 17 (4): 40801.
- 421 6. Kendall, A., Isabelle, M., Bazant-Hegemanrk, F., Hutchings, J., LOrr, L., Babrah, J.,
422 Baker, R., and Stone, N. (2009) Vibrational spectroscopy: a clinical tool for cancer
423 diagnosis. *Analyst* 134: 1029–1045.
- 424 7. Bellisola, G., and Sorio, C. (2012) Infrared spectroscopy and microscopy in cancer
425 research and diagnosis. *Am. J. Cancer Res.* 2 (1): 1–21.
- 426 8. Caine, S., Heraud, P., Tobin, M. J., McNaughton, D., and Bernard, C. C. A. (2012)
427 The application of Fourier transform infrared microspectroscopy for the study of
428 diseased central nervous system tissue. *Neuroimage* 59 (4): 3624–3640.
- 429 9. Sawcer, S., Hellenthal, G., Pirinen, M., Spencer, C. C. A., Patsopoulos, N. A.,
430 Moutsianas, L., Su, Z., Freeman, C., Hunt, S. E., Edkins, S., Gray, E., David, R.,
431 Potter, S. C., Goris, A., Band, G., Oturai, A. B., Strange, A., Comabella, M.,
432 Hammond, N., Kockum, I., Mccann, O. T., Ban, M., Dronov, S., Robertson, N.,
433 Bumpstead, S. J., Lisa, F., International, T., Sclerosis, M., Consortium, G., Case, W.
434 T., and Wtccc, C. C. (2012) Genetic risk and a primary role for cell-mediated immune
435 mechanisms in multiple sclerosis. *Nature* 476 (7359): 214–219.
- 436 10. Lublin, F. D., Reingold, S. C., Cohen, J. A., Cutter, G. R., Sørensen, P. S., Thompson,
437 A. J., Wolinsky, J. S., Balcer, L. J., Banwell, B., Barkhof, F., Bebo, B., Calabresi, P.
438 A., Clanet, M., Comi, G., Fox, R. J., Freedman, M. S., Goodman, A. D., Inglese, M.,
439 Kappos, L., Kieseier, B. C., Lincoln, J. A., Lubetzki, C., Miller, A. E., Montalban, X.,
440 O'Connor, P. W., Petkau, J., Pozzilli, C., Rudick, R. A., Sormani, M. P., Stüve, O.,

- 441 Waubant, E., and Polman, C. H. (2014) Defining the clinical course of multiple
442 sclerosis: The 2013 revisions. *Neurology* 83 (3): 278–286.
- 443 11. Antel, J., Antel, S., Caramanos, Z., Arnold, D. L., and Kuhlmann, T. (2012) Primary
444 progressive multiple sclerosis: part of the MS disease spectrum or separate disease
445 entity? *Acta Neuropathol.* 123 (5): 627–638.
- 446 12. Kutzelnigg, A., and Lassmann, H. (2014) Pathology of multiple sclerosis and related
447 inflammatory demyelinating diseases. *Handb. Clin. Neurol.* 122: 15–58.
- 448 13. Compston, A., and Coles, A. (2008) Multiple sclerosis. *Lancet* 372 (9648): 1502–17.
- 449 14. Kutzelnigg, A., Lucchinetti, C. F., Stadelmann, C., Brück, W., Rauschka, H.,
450 Bergmann, M., Schmidbauer, M., Parisi, J. E., and Lassmann, H. (2005) Cortical
451 demyelination and diffuse white matter injury in multiple sclerosis. *Brain* 128 (11):
452 2705–2712.
- 453 15. Christensen, J. R., Börnsen, L., Ratzer, R., Piehl, F., Khademi, M., Olsson, T.,
454 Sørensen, P. S., and Sellebjerg, F. (2013) Systemic Inflammation in Progressive
455 Multiple Sclerosis Involves Follicular T-Helper, Th17- and Activated B-Cells and
456 Correlates with Progression. *PLoS One* 8 (3).
- 457 16. Wattjes, M. P., Rovira, À., Miller, D., Yousry, T. A., Sormani, M. P., De Stefano, N.,
458 Tintoré, M., Auger, C., Tur, C., Filippi, M., Rocca, M. A., Fazekas, F., Kappos, L.,
459 Polman, C., Barkhof, F., and Montalban, X. (2015) Evidence-based guidelines:
460 MAGNIMS consensus guidelines on the use of MRI in multiple sclerosis - Establishing
461 disease prognosis and monitoring patients. *Nat. Rev. Neurol.* 11 (10): 597–606.
- 462 17. Steinman, L. (2014) Immunology of Relapse and Remission in Multiple Sclerosis.
463 *Annu. Rev. Immunol.* 32 (1): 257–281.
- 464 18. Vargas, D. L., and Tyor, W. R. (2017) Update on disease-modifying therapies for
465 multiple sclerosis. *J. Investig. Med.*
- 466 19. Partridge, M. A., Gopinath, S., Myers, S. J., and Coorsen, J. R. (2016) An initial top-
467 down proteomic analysis of the standard cuprizone mouse model of multiple sclerosis.
468 *J. Chem. Biol.* 9 (1): 9–18.
- 469 20. Ransohoff, R. M. (2012) Animal models of multiple sclerosis: the good, the bad and
470 the bottom line. *Nat Neurosci* 15 (8): 1074–1077.
- 471 21. van der Star, B. J., Vogel, D. Y. S., Kipp, M., Puentes, F., Baker, D., and Amor, S.
472 (2012) In vitro and in vivo models of multiple sclerosis. *CNS Neurol. Disord. Drug*
473 *Targets* 11: 570–88.
- 474 22. Peferoen, L. A. N., Breur, M., van de Berg, S., Peferoen-Baert, R., Boddeke, E. H. W.
475 G. M., van der Valk, P., Pryce, G., van Noort, J. M., Baker, D., and Amor, S. (2016)
476 Ageing and recurrent episodes of neuroinflammation promote progressive
477 experimental autoimmune encephalomyelitis in Biozzi ABH mice. *Immunology* 149

- 478 (2): 146–156.
- 479 23. Behan, P. O., and Chaudhuri, A. (2014) EAE is not a useful model for demyelinating
480 disease. *Mult. Scler. Relat. Disord.* 3 (5): 565–574.
- 481 24. Dutta, R., and Trapp, B. D. (2014) Relapsing and progressive forms of multiple
482 sclerosis. *Curr. Opin. Neurol.* 27 (3): 271–278.
- 483 25. Waller, R., Woodroffe, M. N., Wharton, S. B., Ince, P. G., Francese, S., Heath, P. R.,
484 Cudzich-Madry, A., Thomas, R. H., Rounding, N., Sharrack, B., and Simpson, J. E.
485 (2016) Gene expression profiling of the astrocyte transcriptome in multiple sclerosis
486 normal appearing white matter reveals a neuroprotective role. *J. Neuroimmunol.* 299:
487 139–146.
- 488 26. Farias, A. S., Pradella, F., Schmitt, A., Santos, L. M. B., and Martins-de-Souza, D.
489 (2014) Ten years of proteomics in multiple sclerosis. *Proteomics* 14 (4–5): 467–480.
- 490 27. Del Boccio, P., Rossi, C., di Iorio, M., Cicalini, I., Sacchetta, P., and Pieragostino, D.
491 (2016) Integration of metabolomics and proteomics in multiple sclerosis: From
492 biomarkers discovery to personalized medicine. *Proteomics - Clin. Appl.* 10 (4): 470–
493 484.
- 494 28. Choo, L. P., Jackson, M., Halliday, W. C., and Mantsch, H. H. (1993) Infrared
495 spectroscopic characterisation of multiple sclerosis plaques in the human central
496 nervous system. *Biochim. Biophys. Acta* 1182 (3): 333–337.
- 497 29. LeVine, SM; Wetzel, D. (1998) Chemical analysis of multiple sclerosis lesions by FT-
498 IR microspectroscopy. *Free Radic Biol Med* 25 (1): 33–41.
- 499 30. Poon, K. W., Brideau, C., Teo, W., Schenk, G. J., Klaver, R., Klauser, A. M.,
500 Kawasoe, J. H., Geurts, J. J. G., and Sty, P. K. (2013) Investigation of human multiple
501 sclerosis lesions using high resolution spectrally unmixed CARS microscopy. *Proc.*
502 *SPIE 8565, Photonic Ther. Diagnostics IX* 85654V.
- 503 31. Poon, K. W., Brideau, C., Schenk, G. J., Klaver, R., Klauser, A. M., Kawasoe, J. H.,
504 Geurts, J. J., and Stys, P. K. (2015) Quantitative biochemical investigation of various
505 neuropathologies using high-resolution spectral CARS microscopy. *Proc. SPIE 9305,*
506 *Opt. Tech. Neurosurgery, Neurophotonics, Optogenetics II* 930504.
- 507 32. Heraud, P., Caine, S., Campanale, N., Karnezis, T., McNaughton, D., Wood, B. R.,
508 Tobin, M. J., and Bernard, C. C. A. (2010) Early detection of the chemical changes
509 occurring during the induction and prevention of autoimmune-mediated demyelination
510 detected by FT-IR imaging. *Neuroimage* 49 (2): 1180–1189.
- 511 33. Heraud, P., Caine, S., Campanale, N., Karnezis, T., McNaughton, D., Wood, B. R.,
512 Tobin, M. J., and Bernard, C. C. A. (2010) Early detection of the chemical changes
513 occurring during the induction and prevention of autoimmune-mediated demyelination
514 detected by FT-IR imaging. *Neuroimage* 49 (2): 1180–1189.

- 515 34. Fu, Y., Wang, H., Huff, T. B., Shi, R., and Cheng, J.-X. (2008) Coherent anti-Stokes
516 Raman scattering imaging of myelin degradation reveals a calcium-dependent
517 pathway in lyso-PtdCho-induced demyelination. *J Neurosci Res* 85 (13): 2870–2881.
- 518 35. Fu, Y., Frederick, T. J., Huff, T. B., Goings, G. E., Miller, S. D., and Cheng, J.-X.
519 (2011) Paranodal myelin retraction in relapsing experimental autoimmune
520 encephalomyelitis visualized by coherent anti-Stokes Raman scattering microscopy
521 Paranodal myelin retraction in relapsing experimental autoimmune encephalomyelitis
522 visualized by coherent ant. *J. Biomed. Opt.* 16 (10): 106006–1:10.
- 523 36. Imitola, J., Côté, D., Rasmussen, S., Xie, X. S., Liu, Y., Chitnis, T., Sidman, R. L., Lin,
524 C. P., and Khoury, S. J. (2011) Multimodal coherent anti-Stokes Raman scattering
525 microscopy reveals microglia-associated myelin and axonal dysfunction in multiple
526 sclerosis-like lesions in mice. *J. Biomed. Opt.* 16 (2): 21109.
- 527 37. Wang, C., Wu, C., Popescu, D., Zhu, J., Macklin, W., Miller, R., and Wang, Y. (2011)
528 Longitudinal Near Infrared Imaging of Myelination. *J Neurosci* 31 (7): 2382–2390.
- 529 38. Ryzhikova, E., Kazakov, O., Halamkova, L., Celmins, D., Malone, P., Molho, E.,
530 Zimmerman, E. A., and Lednev, I. K. (2015) Raman spectroscopy of blood serum for
531 Alzheimer's disease diagnostics: specificity relative to other types of dementia. *J*
532 *Biophotonics* 8 (7): 584–596.
- 533 39. Carmona, P., Molina, M., Calero, M., Bermejo-Pareja, F., Martínez-Martín, P., and
534 Toledano, A. (2013) Discrimination analysis of blood plasma associated with
535 Alzheimer's disease using vibrational spectroscopy. *J. Alzheimers. Dis.* 34 (August
536 2015): 911–20.
- 537 40. Peuchant, E., Richard-Harston, S., Bourdel-Marchasson, I., Dartigues, J. F.,
538 Letenneur, L., Barberger-Gateau, P., Arnaud-Dabernat, S., and Daniel, J. Y. (2008)
539 Infrared spectroscopy: a reagent-free method to distinguish Alzheimer's disease
540 patients from normal-aging subjects. *Transl. Res.* 152 (3): 103–112.
- 541 41. Griebe, M., Daffertshofer, M., Stroick, M., Syren, M., Ahmad-Nejad, P., Neumaier, M.,
542 Backhaus, J., Hennerici, M. G., and Fatar, M. (2007) Infrared spectroscopy: A new
543 diagnostic tool in Alzheimer disease. *Neurosci. Lett.* 420 (1): 29–33.
- 544 42. Mordechai, S., Shufan, E., Porat Katz, B. S., and Salman, A. (2017) Early diagnosis of
545 Alzheimer's disease using infrared spectroscopy of isolated blood samples followed
546 by multivariate analyses. *Analyst.*
- 547 43. Eysel, H. H., Jackson, M., Nikulin, A., Somorjai, R. L., Thomson, G. T. D., and
548 Mantsch, H. H. (1997) A novel diagnostic test for arthritis: Multivariate analysis of
549 infrared spectra of synovial fluid. *Biospectroscopy* 3 (2): 161–167.
- 550 44. Esmonde-White, K. A., Mandair, G. S., Raaij, F., Jacobson, J. A., Miller, S., Urquhart,
551 A. G., Roessler, B. J., and Morris, M. D. (2009) Raman Spectroscopy of Synovial

- 552 Fluid as a Tool for Diagnosing Osteoarthritis. *J Biomed Opt* 14 (3): 1–17.
- 553 45. Ildiz, G. O., Arslan, M., Unsalan, O., Araujo-andrade, C., Kurt, E., Karatepe, H. T.,
554 Yilmaz, A., Yalcinkaya, O. B., and Herken, H. (2016) FT-IR spectroscopy and
555 multivariate analysis as an auxiliary tool for diagnosis of mental disorders : Bipolar and
556 schizophrenia cases. *Spectrochim. Acta Part A Mol. Biomol. Spectrosc.* 152: 551–
557 556.
- 558 46. Bélanger, E., Henry, F. P., Vallée, R., Randolph, M. A., Kochevar, I. E., Winograd, J.
559 M., Lin, C. P., and Côté, D. (2011) In vivo evaluation of demyelination and
560 remyelination in a nerve crush injury model. *Biomed. Opt. Express* 2 (9): 2698–708.
- 561 47. Shi, Y., Sun, W., McBride, J. J., Cheng, J. X., and Shi, R. (2011) Acrolein induces
562 myelin damage in mammalian spinal cord. *J. Neurochem.* 117 (3): 554–564.
- 563 48. Bégin, S., Bélanger, E., Laffray, S., Aubé, B., Chamma, É., Bélisle, J., Lacroix, S., De
564 Koninck, Y., and Côté, D. (2013) Local assessment of myelin health in a multiple
565 sclerosis mouse model using a 2D Fourier transform approach. *Biomed. Opt. Express*
566 4 (10): 2003.

Table 1 Studies considered in this literature review. Sample specimen type and numbers included are indicated as well as the publication year and the spectroscopic technique used.

Authors	Year	Tissue Sample species	No. samples	Spectroscopic technique
Choo <i>et al.</i>	1993	Human	3	FTIR
LeVine <i>et al.</i>	1998	Human	10	FTIR
Fu <i>et al.</i>	2007	Mice	-	CARS
Heraud <i>et al.</i>	2010	Mice	12	FTIR
Belanger <i>et al.</i>	2011	Mice	14	CARS
Shi <i>et al.</i>	2011	Guinea pigs	-	CARS
Wang <i>et al.</i>	2011	Mice	7	NIRF
Imitola <i>et al.</i>	2011	Mice	-	CARS
Fu <i>et al.</i>	2011	Mice	-	CARS
Begin <i>et al.</i>	2013	Mice	4	CARS
Poon <i>et al.</i>	2013	Human	5	CARS
Hu <i>et al.</i>	2014	<i>Xenopus laevis</i>	-	SRS
Marro <i>et al.</i>	2014	Murine retinal organotypic cultures	12	Raman Spectroscopy
Poon <i>et al.</i>	2015	Human	6	CARS

Figure 1. Mean FTIR spectra for four post-mortem samples analysed in the preliminary study: chronic lesion (blue), active lesion (red), NAWM (green) and control (black). All samples were subjected to FTIR analysis at the Focas Research Institute, DIT, using a Perkin Elmer Spotlight 400N FTIR imaging system, incorporating a liquid nitrogen cooled mercury cadmium telluride 16x1, 6.25 μm pixel array detector, and acquired by the Spectral Image software. FTIR images from the tissue sections (10 μm sections) mounted on CaF_2 slides were recorded over the range 4000-800 cm^{-1} in transmittance mode with a resolution of 4 cm^{-1} and interferometer speed of 1.0 cm^{-1} /second at continuously varying magnification. The scans per pixel for background were 120 and, for images, 16 per pixel respectively. Spectroscopic data analysis was carried out in Matlab, version R2013 (Mathworks, CA, USA) according to protocols developed and routinely used in-house at DIT.

Figure 2. PCA of the four post-mortem samples FTIR data. (A) 2-D PCA scatterplot showing a separation between chronic (blue) and active lesion (red) and, NAWM (green) and control (black). (B) PC1 loading, responsible for the separation, is negatively dominated by peaks assigned to lipids around 2800-3000 cm^{-1} .

Figure 3. PCA of the NAWM and control FTIR data. (A) The two dimensional PCA plot shows a separation between NAWM (black) and control (green) FTIR spectra in PC1 which explains 80.63% of the variation found in the data. (B) The PC1 loading is negatively dominated by peaks assigned to lipids around 2800-3000 cm^{-1} .

Figure 4. PCA of the four post-mortem samples Raman spectroscopy data. (A) 2-D PCA scatterplots showing a separation between chronic (blue) and active lesion (red) and, NAWM (green) and control (black). (B) PC1 and PC3 loadings, responsible for the separation.

Figure 1

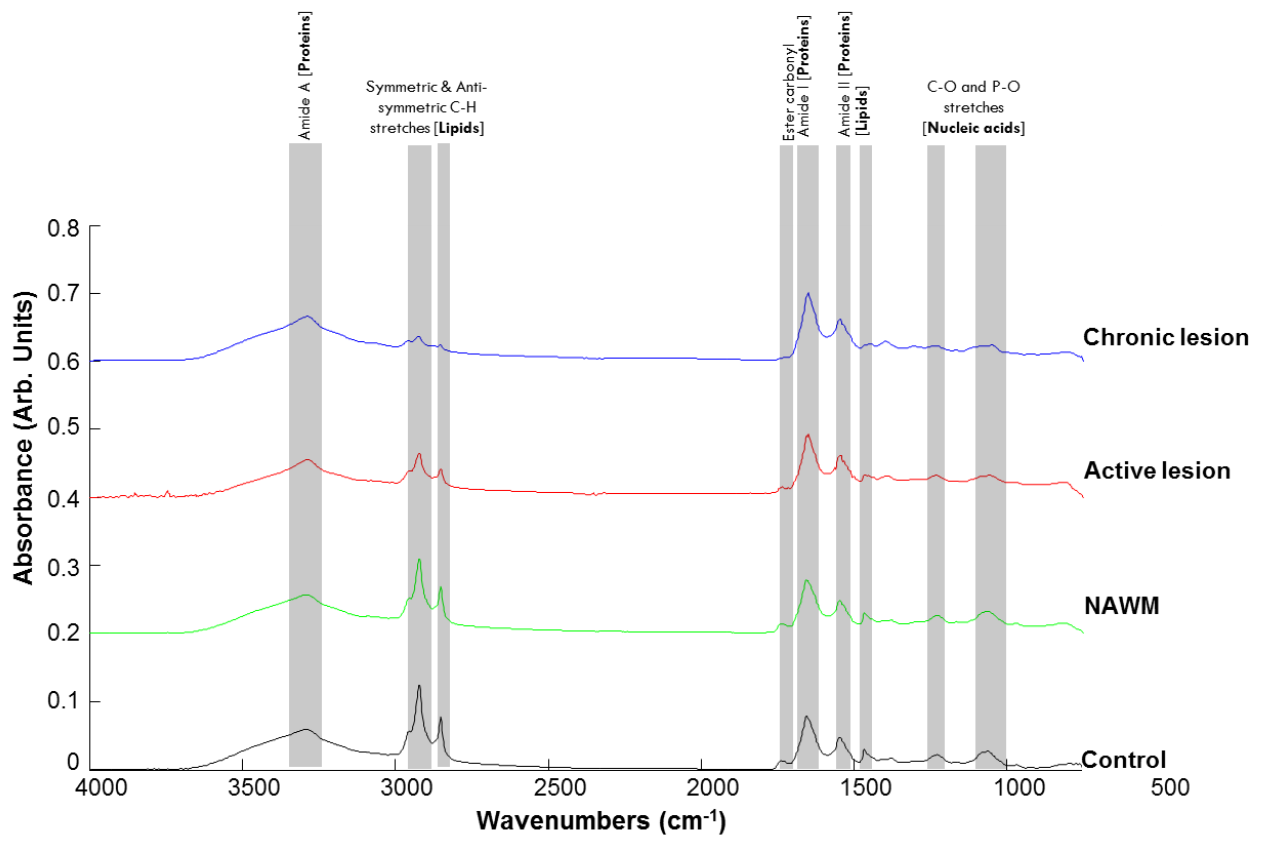
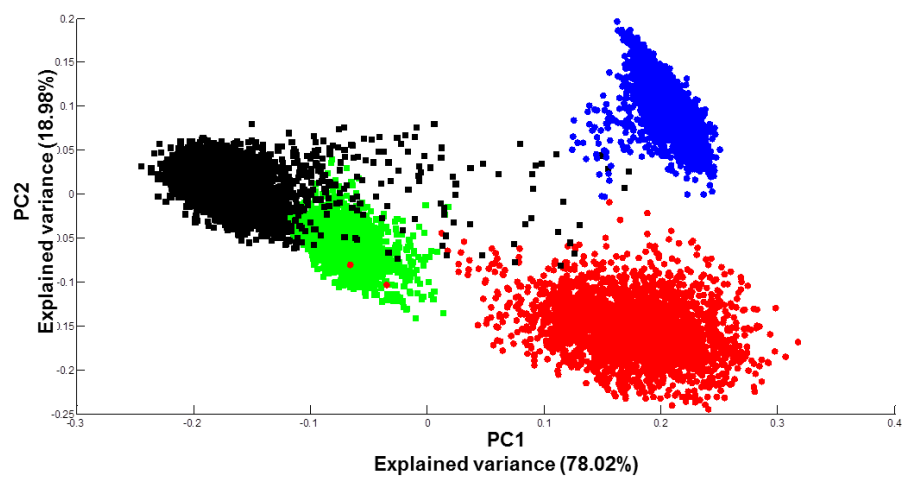


Figure 2

A



B

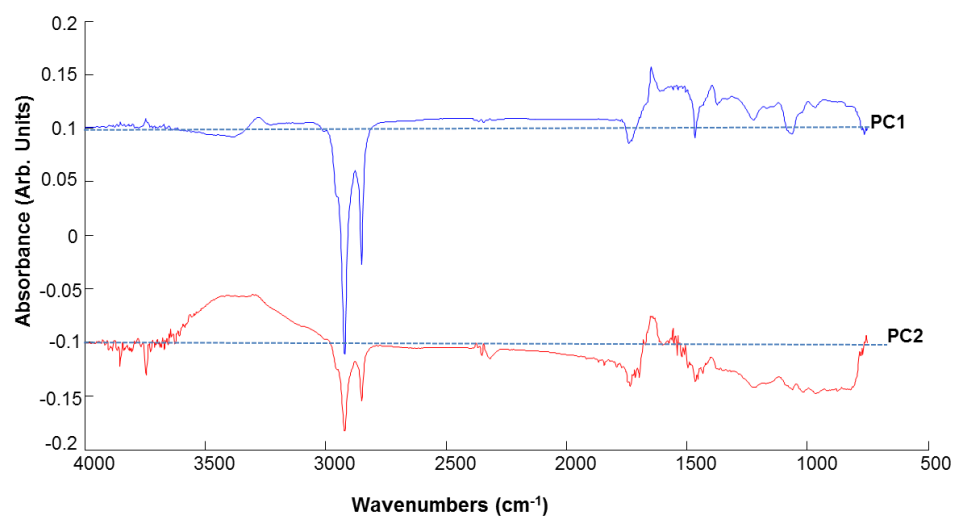
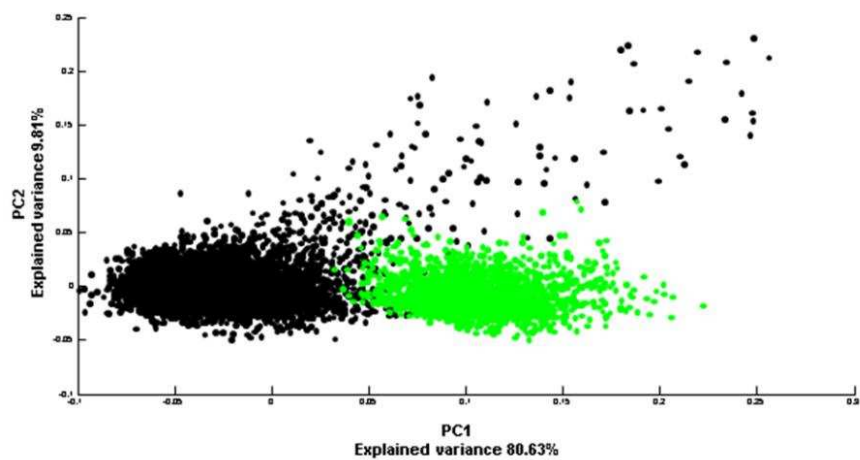


Figure 3

A



B

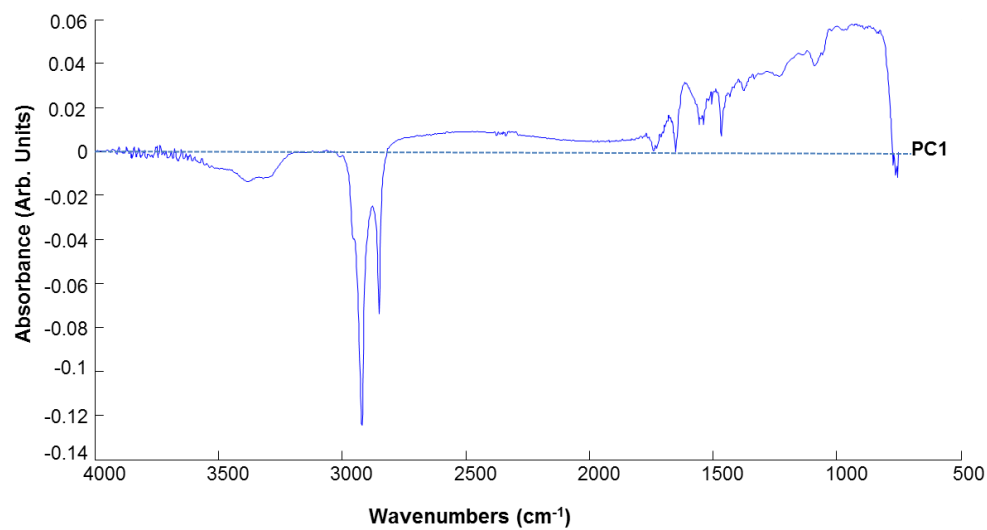
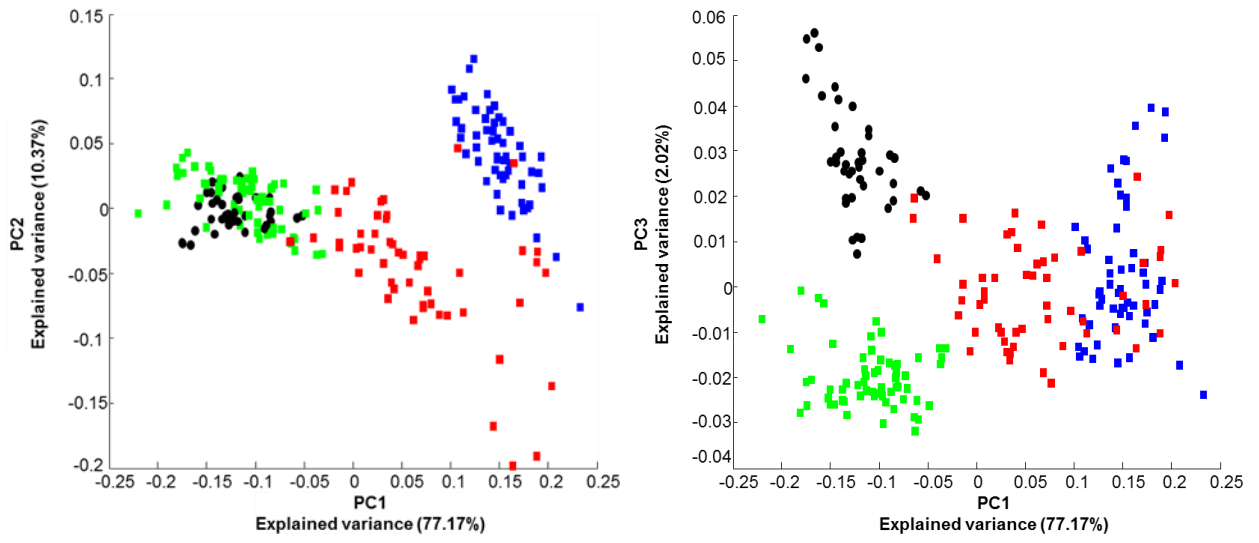
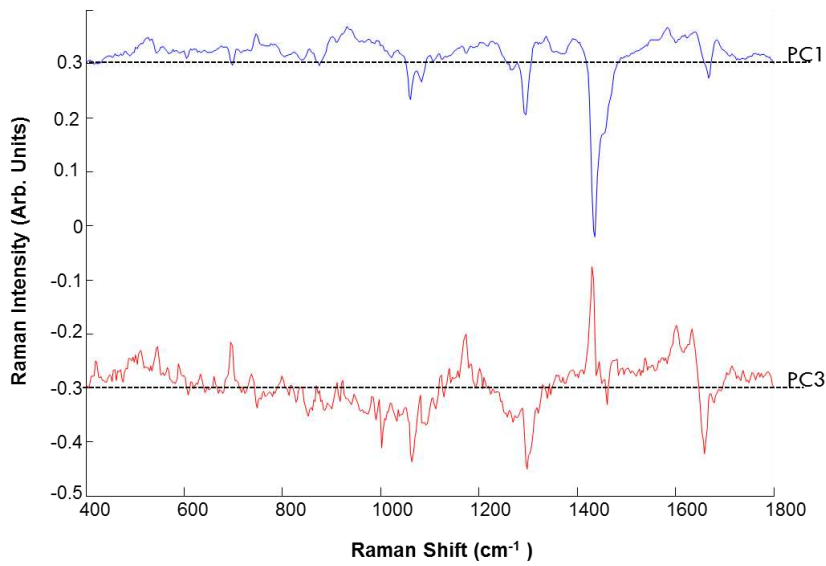


Figure 4

A



B



567